nature electronics

ARTICLES

https://doi.org/10.1038/s41928-021-00584-y

Self-biased magnetoelectric switching at room temperature in three-phase ferroelectric–antiferromagnetic–ferrimagnetic nanocomposites

Rui Wu[1,11] ✉, Di Zhang[2], Tuhin Maity[1,12] ✉, Ping Lu[3], Jie Yang[4], Xingyao Gao[2], Shishun Zhao[5], Xiucheng Wei[6], Hao Zeng[6], Ahmed Kursumovic[1], Guang Tian[4], Weiwei Li[1], Chao Yun[1], Yongqiang Wang[7], Zengyao Ren[8], Ziyao Zhou[5], Ming Liu[5], Kelvin H. L. Zhang[9], Quanxi Jia[10], Jinbo Yang[4], Haiyan Wang[2] and Judith L. MacManus-Driscoll[1] ✉

Magnetoelectric systems could be used to develop magnetoelectric random access memory and microsensor devices. One promising system is the two-phase 3-1-type multiferroic nanocomposite in which a one-dimensional magnetic column is embedded in a three-dimensional ferroelectric matrix. However, it suffers from a number of limitations including unwanted leakage currents and the need for biasing with a magnetic field. Here we show that the addition of an antiferromagnet to a 3-1-type multiferroic nanocomposite can lead to a large, self-biased magnetoelectric effect at room temperature. Our three-phase system is composed of a ferroelectric $Na_{0.5}Bi_{0.5}TiO_3$ matrix in which ferrimagnetic $NiFe_2O_4$ nanocolumns coated with antiferromagnetic p-type NiO are embedded. This system, which is self-assembled, exhibits a magnetoelectric coefficient of up to 1.38×10^{-9} s m^{-1}, which is large enough to switch the magnetic anisotropy from the easy axis ($K_{eff} = 0.91 \times 10^4$ J m^{-3}) to the easy plane ($K_{eff} = -1.65 \times 10^4$ J m^{-3}).

Magnetoelectric (ME) coupling between ferro-/ferrimagnetic (FM) and ferroelectric (FE) orders allows magnetism to be controlled by an electric field, and vice versa[1,2]. As a result, magnetoelectric random access memory (MeRAM) devices could potentially have a write power consumption that is about two orders of magnitude lower than electric-current-driven spintronic memory devices[3]. However, single-phase materials with ME coupling are rare and have many inherent drawbacks including low magnetic and/or electric ordering temperature and weak ME coupling strength[4].

Multiferroic nanocomposites comprising FM and FE materials could potentially be used to address these problems[5]. In such composites, the FE and FM materials can interact with each other via internal strain coupling. A typical form of multiferroic nanocomposite is the 3-1-structured nanocomposite[6,7], in which a one-dimensional magnetic column is embedded in a three-dimensional continuous FE matrix. In this structure, the effective strain is along the out-of-plane (OOP) direction, and it is largely free from the in-plane (IP) substrate clamping effect. The nanocomposites could therefore exhibit an ME response that is much larger than that of their layered counterparts such as 2-2-type systems, where the ME effect is very weak due to the substrate clamping effect[8,9].

However, the 3-1-type systems developed to date have not given rise to useful ME effects. This is due to the limited exploration of the selected materials in this structure. In particular, the FE materials used either have a high Curie temperature (T_C) or low leakage, but not both[7,10]— and both properties are needed to deliver high-temperature low-loss devices. Similarly, the FM materials used do not have a high magnetoelastic effect, high resistance and relatively soft magnetism needed to deliver devices with a large ME effect and low loss, which can be switched without an external magnetic field (that is, self-biased ME).

Antiferromagnetic (AFM) materials have played an essential role in traditional spintronic devices as pinning layers[11] and are also used in emerging spintronic devices due to their ultrafast (approximately terahertz) dynamics and high stability to external field[12]. However, the use of materials in multiferroic nanocomposites to tailor the ME properties has largely been overlooked. AFM/FE $BiFeO_3$ (BFO)—a single-phase multiferroic AFM material—has been used in 3-1-type systems[13], but high leakage makes it challenging to exploit its intrinsic properties.

In this Article, we report an FE–AFM–FM three-phase 3-1-structured multiferroic nanocomposite system of $Na_{0.5}Bi_{0.5}TiO_3$–NiO–$NiFe_2O_4$ (NBT–NiO–NFO). $Na_{0.5}Bi_{0.5}TiO_3$ (NBT) is chosen

---

[1]Department of Materials Science & Metallurgy, University of Cambridge, Cambridge, UK. [2]Materials Engineering, Purdue University, West Lafayette, IN, USA. [3]Sandia National Laboratories, Albuquerque, NM, USA. [4]State Key Laboratory for Artificial Microstructure and Mesoscopic Physics, School of Physics, Peking University, Beijing, People's Republic of China. [5]Electronic Materials Research Laboratory, Key Laboratory of the Ministry of Education & International Center for Dielectric Research, Xi'an Jiaotong University, Xi'an, People's Republic of China. [6]Department of Physics, University at Buffalo—the State University of New York, Buffalo, NY, USA. [7]Materials Science and Technology Division, Los Alamos National Laboratory, Los Alamos, NM, USA. [8]School of Materials Science and Engineering, University of Science and Technology Beijing, Beijing, People's Republic of China. [9]State Key Laboratory of Physical Chemistry of Solid Surfaces, College of Chemistry and Chemical Engineering, Xiamen University, Xiamen, People's Republic of China. [10]Department of Materials Design and Innovation, University at Buffalo—the State University of New York, Buffalo, NY, USA. [11]Present address: Beijing Academy of Quantum Information Sciences, Beijing, People's Republic of China. [12]Present address: School of Physics, Indian Institute of Science Education and Research Thiruvananthapuram, Thiruvananthapuram, India. ✉e-mail: ruiwu001@baqis.ac.cn; tuhin@iisertvm.ac.in; jld35@cam.ac.uk

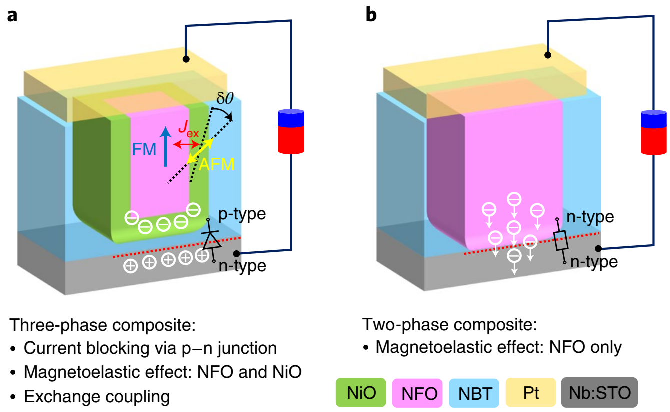

Fig. 1 | Schematic of a comparison between three-phase and two-phase nanocomposites. **a**, In the NBT–NiO–NFO three-phase nanocomposite: p-type NiO and NBT separate the NFO from contacting the Nb:STO substrate and block the leakage current via the p–n junction formed at the film–substrate interface; the exchange coupling between NiO and NFO yields a large room-temperature EB effect; the NiO presents a large magnetoelastic effect and contributes to the overall ME effect via exchange coupling with NFO. **b**, In the NBT–NFO two-phase nanocomposite, the lack of a p–n junction leads to a large leakage current; the ME effect is contributed by NFO only.

as the FE material because of its low leakage and high T_C (603 K); $NiFe_2O_4$ (NFO) is chosen as the FM material because of its relatively soft magnetism; and NiO is the chosen as the AFM material because of its high Néel temperature (525 K) and large exchange coupling to FM materials. NFO and NiO are also chemically and structurally compatible.

A large, self-biased (zero applied magnetic field) ME effect at room temperature is achieved in the NBT–NiO–NFO system. The ME effect is ascribed to three critical features created through the addition of NiO (Fig. 1): the leakage is strongly suppressed by the introduction of p-type NiO; the exchange coupling between the AFM NiO and FM NFO produces a large exchange bias (EB) effect at room temperature; the large magnetoelastic effect of the AFM NiO induces a larger ME coupling than in a two-phase composite system in which the NiO shell is absent. With our NBT–NiO–NFO three-phase 3-1-type system, in situ control of magnetic anisotropy using an electric field is demonstrated with an ME coefficient of up to $1.38\times10^{-9}\,\mathrm{s\,m^{-1}}$. This value is higher than has been previously observed in two-phase systems[14]. Moreover, the largest ME effect in our system occurs at zero applied magnetic field.

Thin-film fabrication

NBT–NiO–NFO and NBT–NFO 3-1-structured nanocomposite films were prepared using pulsed laser deposition. In both films, the volume fraction of NBT is kept the same at 50%. For the NBT–NiO–NFO films, to clearly understand the influence of NiO in the composites, two compositions were studied with two different NiO–NFO ratios, namely, 3:1 and 3:2 (referred to as NNN-31 and NNN-32, respectively). Reference NBT–NFO (1:1 by volume ratio) 3-1-structured nanocomposite films were prepared and are referred to as NN. Good chemical stoichiometry of the NBT phase and highly epitaxial growth of our nanocomposite films were confirmed by the Rutherford backscattering spectrometry (RBS) measurements (Supplementary Fig. 1) and X-ray diffraction (XRD) Omega-2Theta scans (Supplementary Fig. 2a,b), respectively.

Leakage and FE characterizations

As shown in Fig. 2a, we measured the current density versus electric field (*J*–*E*) curves of samples NN, NNN-32 and NNN-31, all having similar thicknesses, to determine the impact of the addition of NiO on reducing the electric leakage. Among the three samples, NN shows a fairly symmetric *J*–*E* curve, with a high current density, that is, $J=2\times10^{-3}\,\mathrm{A\,cm^{-2}}$ at $E=\pm200\,\mathrm{kV\,cm^{-1}}$, while in samples NNN-32 and NNN-31, the leakage currents were largely suppressed. At an electric field of $-200\,\mathrm{kV\,cm^{-1}}$, the leakage *J* of both three-phase samples is $\sim1\times10^{-6}\,\mathrm{A\,cm^{-2}}$, which is more than three orders of magnitude lower than that of the NN sample, and the difference increases sharply with an increasing electric field. The leakage current is notably lower compared with the well-known 3-1-type nanocomposites, such as BFO–CFO (refs. [10,14]) with $J=1\times10^{-4}\,\mathrm{A\,cm^{-2}}$ at $-200\,\mathrm{kV\,cm^{-1}}$ and PZT–CFO (ref. [15]) with $J=5\times10^{-3}\,\mathrm{A\,cm^{-2}}$ at $-100\,\mathrm{kV\,cm^{-1}}$. In the positive electric field direction, the leakage currents of three-phase samples are still smaller than that of the two-phase sample (below $\sim150\,\mathrm{kV\,cm^{-1}}$). However, the current density sharply increases with an increase in the positive electric field in these two samples, indicative of a p–n junction formed in these samples, which we will discuss later. It is noted that the *J*–*E* curves, especially under the positive electric field, always show a slight difference in the different samples even with the same composition, depending on sample preparation and electrode size, as well as measurement history, as detailed in Supplementary Figs. 3 and 4. However, the difference between the three-phase samples and two-phase samples is robust.

Figure 2b gives the FE polarization versus electric field (*P*–*E*) loops of the three samples. It can be found that the leakage characteristics shown in the *P*–*E* loops are consistent with the *J*–*E* curves, that is, NN > NNN-31 > NNN-32. The polarization (*P*), remanence polarization (P_R) and coercive field (E_C) of the three samples are similar considering the effect of leakage, which indicates that the FE properties of the NBT phase in these samples are basically the same. Piezoresponse force microscopy (PFM) images shown in Supplementary Fig. 5 demonstrate that the FE phase is the NBT matrix.

Microstructural analysis

To explore the mechanism of leakage suppression in the three-phase composite films, scanning transmission electron microscope (STEM) characterization was carried out. First, a 50 nm NNN-31 film sample was used to investigate the growth mechanism of the three-phase composites. The plan-view high-angle annular dark-field (HAADF) image and energy-dispersive X-ray spectroscopy (EDX) elemental distribution shown in Fig. 3a reveals that the NFO cores are surrounded by thin NiO shells for each NiO–NFO nanocolumn. Figure 3b shows the cross-sectional HAADF and EDX images. It can be seen that the NFO pillars are coated with 'bowl-like' NiO shells surrounded by the NBT matrix. Based on the high-resolution STEM (HRSTEM) image, it is found that the bottom of the NiO–NFO column does not directly contact the Nb:STO substrate. Instead, an ultrathin NBT layer was first formed on the substrate and then the NiO–NFO nanocolumn was grown and 'floated' above within the NBT matrix.

Next, the STEM analyses on the thicker (200 nm) NNN-31 and NN samples were conducted. By comparing the HAADF and EDX images shown in Fig. 3c,f, it is clear that the NNN-31 film contains three phases, while the NN film contains only two phases, as shown in both STEM images. The HRSTEM image (Fig. 3d) also indicates the indirect contact between NiO and Nb:STO substrate. In contrast, from the HRSTEM image of the NN film (Fig. 3g), the direct nucleation and growth of NFO pillars on the Nb:STO substrate is observed, forming a clear and sharp NFO–Nb:STO interface.

A continuous NBT interlayer is further confirmed by the EDX analysis at the film–substrate interface, as shown in Supplementary Fig. 6. The formation of this special structure is related to the thermodynamic conditions, including the surface, interface and elastic strain energies of the two immiscible phases on a certain substrate[16]. The assembly of the NBT layer under the NFO/NiO

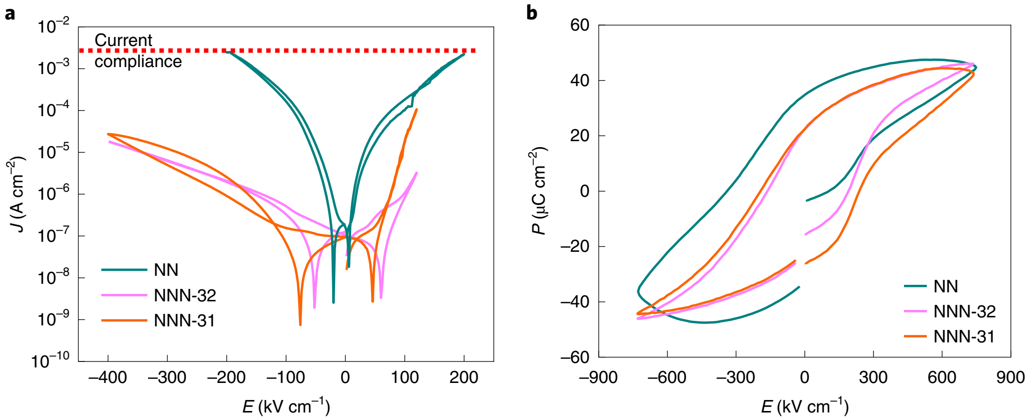

Fig. 2 | Characterizations of leakage. a,**b**, *J*–*E* curves (**a**) and *P*–*E* loops (**b**) of samples NN, NNN-32 and NNN-31 with the same thickness of ~200 nm.

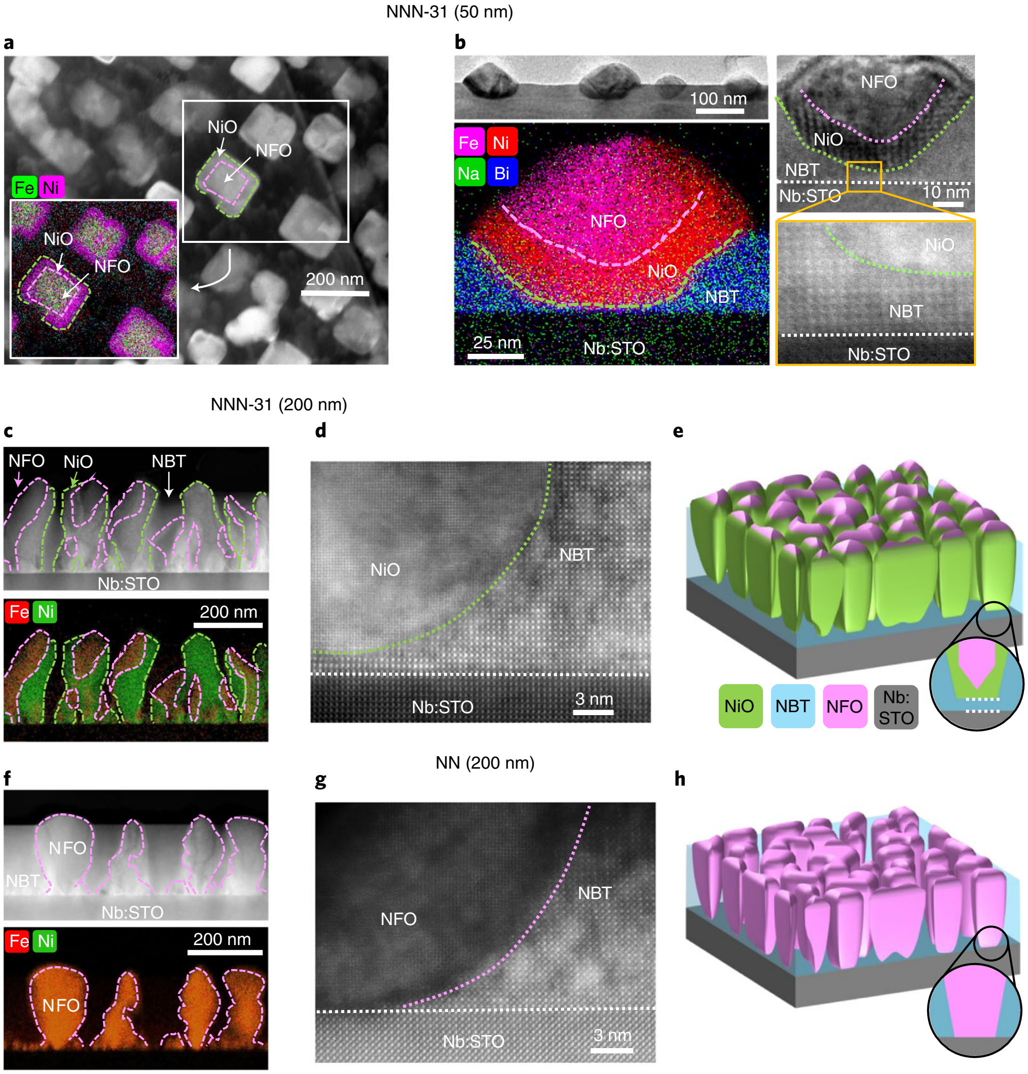

Fig. 3 | STEM characterizations. a,**b**, Plan-view HAADF and EDX images (**a**) and the cross-sectional EDX image and TEM image (**b**) for a 50-nm-thick NNN-31 sample. **c**–**e**, Cross-sectional HAADF image and EDX image (**c**), high-resolution STEM image (**d**) and microstructure schematic (**e**) for a 200-nm-thick NNN-31 sample. **f**–**h**, Cross-sectional HAADF image and EDX image (**f**), high-resolution STEM image (**g**) and microstructure schematic (**h**) for a 200-nm-thick NN sample.

nanocolumn should correspond to a reduction in the total surface energy of the four-phase system (three-phase film and substrate). This is supported by density functional theory (DFT) calculations shown in Supplementary Figs. 7 and 8, which reveal a larger binding energy at the NBT–STO interface than at the NiO–STO interface, and larger binding energy at the NiO–NBT interface than at

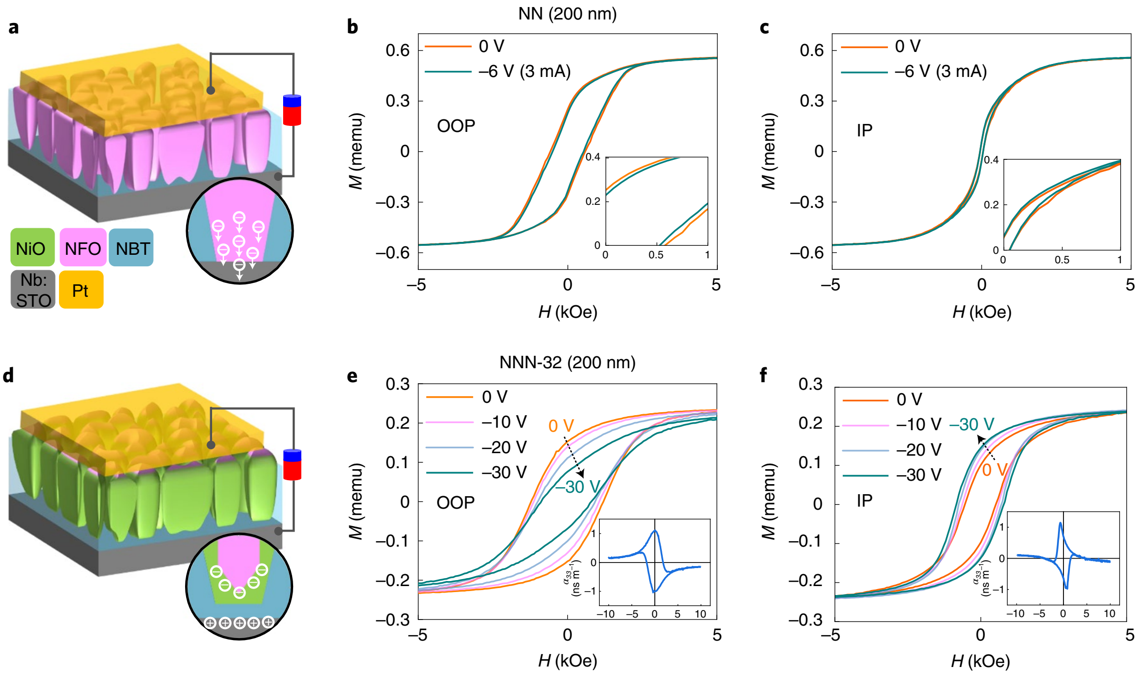

Fig. 4 | Magnetic hysteresis loops measured with in situ electric voltage. a, Schematic of the in situ electric field control of magnetism in the NN nanocomposite, where the inset shows the leakage current through the film–substrate interface. **b**,**c**, Hysteresis loops of the NN sample in the OOP (**b**) and IP (**c**) directions under 0 V and −6 V, where the insets show zoomed-in views of the hysteresis loops in the first quadrant. **d**, Schematic of the in situ electric field control of magnetism in the NNN-32 three-phase nanocomposite, where the inset shows the leakage current blocked at the film–substrate interface. **e**,**f**, Hysteresis loops of NNN-32 in the OOP (**e**) and IP (**f**) directions under different voltages, where the insets show the ME coefficients in both directions calculated from the hysteresis loops measured at 0 V and −30 V.

the NFO–NBT interface. We also noted that this interlayer feature is absent in other 3-1-structured nanocomposites, such as BFO–CFO grown on Nb:STO (ref. [17]) and BFO–MnFe$_2$O$_4$ on STO (ref. [18]), but it was recently observed in the (111)-oriented BFO–CFO grown on SrRuO$_3$ (SRO) (ref. [19]), where the CFO phase is separated from SRO by a very thin BFO (<2 nm) layer. Based on the TEM results, schematics of the microstructures of the NNN-31 three-phase and NN two-phase nanocomposite films are presented in Fig. 3e,h, where the insets show the zoomed-in views of the interfacial area between the nanocolumn and substrate. The observed structure was further elaborated by atomic force microscopy (AFM) images (Supplementary Fig. 2c–f).

Geometric phase analysis was conducted to demonstrate the strain states within the NNN-31 and NN nanocomposite films. As shown in Supplementary Figs. 9 and 10, from both IP and OOP strain maps, no strong local strained area is found at the NBT–Nb:STO interfaces because of the close lattice parameters of Nb:STO and NBT, which result in a coherent interface. On the other hand, the strong strain contrast shown in the NiO nanocolumn phase indicates incoherent strain at the NiO–NBT interface due to the large lattice mismatch. Similar results are observed for the NN film.

Leakage mechanism analysis

Now we show that the NiO shell, as well as the NBT interlayer observed in the HRSTEM image of the three-phase nanocomposite films, play an important role in suppressing the leakage current. First, we ascribe the asymmetric J–E curves to the rectifying effect of the p–n junction at the interface between the film and Nb:STO substrate. The p-type character of the NBT film is demonstrated by the positive Hall coefficient of a 250-nm-thick NBT film grown on the STO substrate, as shown in Supplementary Fig. 11. Moreover, a rectifying current–voltage curve was observed in an NBT film of thickness less than 5 nm grown on Nb:STO(001) (Supplementary Fig. 12), indicating that a p–n junction can form at the NBT–Nb:STO interfaces, even with an ultrathin NBT layer. Nonetheless, due to the limited thickness of NBT at the bottom of the nanocolumns (down to 2 nm), the depletion layer can extend into the NiO layer, which is a well-known p-type transparent semiconductor[20]. From the symmetric characteristics of the J–E curve of the NN sample, it can be inferred that the leakage current is mostly through the NFO columns due to the lack of the p–n junction there, which is confirmed using conductive AFM, as shown in Supplementary Fig. 13. Hence, the p–n junction created between the n-type Nb:STO and p-type NBT–NiO layers in the three-phase samples suppresses the leakage in these films.

ME measurements

To study the ME effect in these samples, the hysteresis loops were measured in the OOP and IP directions of the NN and NNN-32 samples, with different in situ electric voltages applied using the configurations shown in Fig. 4a,d, respectively. Both 3-1-structured nanocomposite films show obvious perpendicular magnetic anisotropy (PMA), that is, the OOP hysteresis loop has a larger coercivity (H_C) and remanent magnetization (M_R) than those of the IP hysteresis loop. This can be expected due to the compressive strain in the NFO or NiO–NFO columns and a negative magnetoelastic coefficient in the (001) direction of NFO.

With the application of a voltage of −6 V on the NN sample, it is observed that both H_C and M_R values measured in the OOP and IP directions are slightly changed, as shown in Fig. 4b,c, that is, M_R and H_C in the OOP direction get smaller, while M_R of the IP hysteresis loop gets slightly larger (although the change in H_C in this direction can be ignored). Thus, we can infer that on the application of voltage, the magnetization of the NFO nanocolumns undergoes a very slight rotation from the OOP direction to the IP direction. The ME coefficient obtained in this NN sample at the voltage of −6 V shows

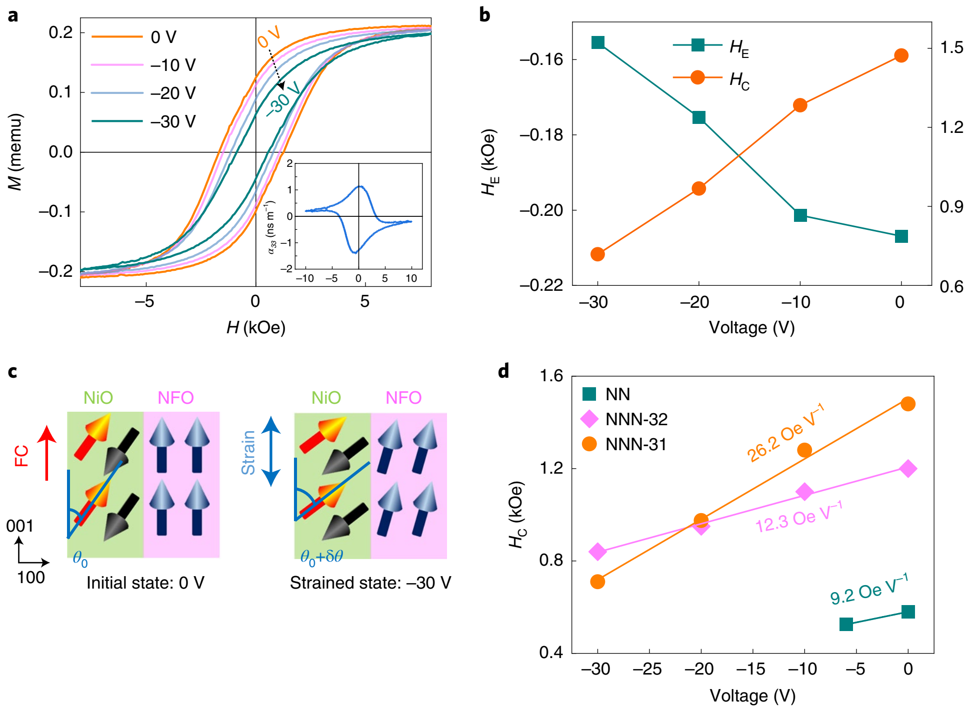

Fig. 5 | Dependence of EB effect on the applied voltage. a, Hysteresis loops of the NNN-31 sample measured with different applied voltages. The inset shows the ME coefficient as a function of different magnetic fields obtained from the magnetization difference between the hysteresis loops under a voltage of −30 V and 0 V. **b**, Electric voltage dependence of H_C and H_E. **c**, Schematic of the magnetic structure in NiO–NFO nanocolumns at different voltages, with the green and pink areas representing NiO and NFO, respectively. **d**, Voltage coefficients of H_C of the NN, NNN-32 and NNN-31 samples.

a maximum value of 0.8×10^{-9} s m^{-1}, as shown in Supplementary Fig. 14. However, owing to the leakage problem in the NN films, the leakage current of the sample at the voltage of −6 V reaches the pre-set current compliance of 3 mA (which was adopted to suppress the Joule heating effect in the system, which corresponds to a current density of 2×10^{-3} A cm^{-2}), thus failing to give an obvious converse ME effect. The ME coupling in this sample is also revealed by the change in ferromagnetic resonance (FMR) on the application of different voltages. As shown in Supplementary Fig. 15a–d, the resonance field of the NN sample can be reversibly tuned by the voltage. However, as shown in Supplementary Fig. 15e,f, due to the weak FMR signal for the NNN-32 sample, the ME effect cannot be detected in the NNN-32 sample using FMR.

Unlike the NN samples, owing to suppressed leakage, the NNN-32 sample shows a remarkable ME effect when the voltage is changed from 0 V to −30 V. As shown in Fig. 4e, with an increase in voltage, both H_C and M_R decrease simultaneously in the OOP hysteresis loops, while the change in IP hysteresis loops shown in Fig. 4f exhibits an opposite trend. More obviously, we observed voltage-induced switching of the PMA. At 0 V, the OOP hysteresis loop has a larger H_C and M_R than those of the IP hysteresis loop. However, on applying a voltage of −30 V, H_C (0.79 kOe) and M_R/M_S (M_S is the saturation magnetization) ratio (0.35) in the OOP hysteresis loop become smaller than those in the IP hysteresis loop, which shows an H_C of 0.83 kOe and M_R/M_S ratio of 0.60. This indicates that at −30 V, the IP direction is more preferred for magnetization than the OOP direction.

From the area enclosed by the hysteresis loops along different directions, the effective magnetic anisotropy coefficient K_{eff} can be determined[21,22]. As shown in Supplementary Fig. 16, this area shows a linear dependence on the applied voltage, yielding K_{eff} varying from 0.91×10^4 J m^{-3} at 0 V to -1.65×10^4 J m^{-3} at −30 V, confirming the magnetic anisotropy switching from easy axis to easy plane. It is also noted that the strain-induced anisotropy change is much larger than the first-order magnetocrystalline anisotropy constant of the bulk NFO, that is, $K_1 = -0.7\times10^4$ J m^{-3} (ref. [23]). The switching of the anisotropy can potentially enable a deterministic magnetization reversal with the help of pulsed electric voltages[24,25]. The maximum ME coefficients α_{33} in the OOP and IP directions are 1.11×10^{-9} s m^{-1} and 1.14×10^{-9} s m^{-1}, respectively, which are larger than the values obtained in the NN sample in both directions.

Voltage-dependent EB

In addition to suppressing the leakage current, the introduction of AFM NiO can also generate EB effects in three-phase nanocomposites[26]. The EB effect is among the major mechanisms for the ME effect because modifications in the AFM spin on the application of an electric field can lead to changes in the magnetic properties of the FM component due to the exchange coupling between them[5]. Supplementary Fig. 17a shows the hysteresis loops of NNN-31 with zero field cooling (ZFC) and field cooling (FC), where the FC hysteresis loop was measured by cooling the sample from 600 K to 300 K under a magnetic field of +10 kOe along the OOP direction. It is found that the FC hysteresis loop shows an EB field of −0.46 kOe and a strongly increased H_C. The temperature dependence of the EB effect shown in Supplementary Fig. 17c,d indicates that EB survives up to 400 K. However, in the NNN-32 sample, due to the lower NiO content, there is only very small EB ($H_E \approx 0.07$ kOe) at room temperature (Supplementary Fig. 18).

Electric voltage control of the EB effect was next investigated in the NNN-31 film. To eliminate the influence of a training effect, the sample was first magnetized repeatedly under a magnetic field of ±10 kOe before applying the voltage. After the training, the hysteresis loop changed very little with further magnetic field cycles.

Figure 5a shows the magnetic hysteresis loops measured under different voltages. As the voltage increases, the trends in H_C and H_E are shown in Fig. 5b. The H_C value decreases from 1.47 kOe to 0.72 kOe with a voltage increase from 0 V to −30 V, indicating switching of the PMA in the NFO. The H_E value also shows a close dependence on the applied voltage. With an increase in the voltage from 0 V to −30 V, H_E decreases from −0.207 kOe to −0.156 kOe. The EB also yields an asymmetric field dependence of the ME coefficient, as shown in the inset of Fig. 5a. This gives a larger ME coefficient at the left branch of the hysteresis ($1.38\times10^{-9}\,\mathrm{s\,m^{-1}}$) than that at the right branch ($1.14\times10^{-9}\,\mathrm{s\,m^{-1}}$). These values are both higher than that of the NNN-32 sample, that is, $1.11\times10^{-9}\,\mathrm{s\,m^{-1}}$ in the OOP direction. We ascribe this high ME coefficient to the synergistic effect from both NFO and NiO phases. The higher ME coefficient in NNN-31 than NNN-32 is due to the larger fraction of NiO in NNN-31. Most importantly, it is found that the ME coefficient reaches its maximum value exactly at zero magnetic field at the left branch. This kind of ME effect is usually known as a self-biased ME effect[27,28], which enables a markedly larger ME effect to be obtained at zero applied external magnetic field. This will reduce the operation energy further. In comparison, similar or smaller coefficients were observed in other multiferroic 3-1-type structures, but with a relatively larger magnetic field applied (for example, $\alpha_{33}=1.25\times10^{-9}\,\mathrm{s\,m^{-1}}$ was reported in the NBT–CFO system at a magnetic field of $H_{\mathrm{d.c.}}=3\,\mathrm{kOe}$ (ref. [14])).

The Meiklejohn and Bean (M–B) model[29] gives the simple relation $H_E\approx\cos\theta$ for EB systems, where θ is the angle between the magnetic field and uncompensated AFM net spins at the interface. Hence, the change in H_E with voltage can only originate from the rotation of uncompensated interfacial AFM spins, which is related to the Néel vector of NiO, towards the IP direction caused by the strain-induced magnetoelastic effect in NiO. Further, for NFO, there is a change in magnetization due to voltage-induced strain on NFO from NBT via NiO. Figure 5c illustrates the change in magnetic anisotropy for both NFO core and NiO shell with voltage-induced strain from the NBT phase. The spin reorientation of NiO induced by the vertical strain change will be discussed in the last part of this paper.

To find out the impact of NiO on the ME effect, H_C as a function of the applied voltage is given in Fig. 5d for the three samples, and the slope obtained from the linear fit is defined as the voltage coefficient of H_C. It is found that as the volume ratio of NiO increases, the voltage coefficient also increases from $9.1\,\mathrm{Oe\,V^{-1}}$ in the two-phase NN sample to $12.3\,\mathrm{Oe\,V^{-1}}$ in the three-phase NNN-32 sample and finally reaches $26.2\,\mathrm{Oe\,V^{-1}}$ in the three-phase NNN-31, with the maximum volume ratio of NiO. It is also found that the voltage coefficient was not enhanced by the FC process because a very similar value was obtained in the NNN-31 sample with ZFC, that is, $27.6\,\mathrm{Oe\,V^{-1}}$ (Supplementary Fig. 19). This trend is consistent with the enhancement in ME coefficient in the nanocomposites with increasing NiO fraction and can be explained by the exchange coupling between NFO and NiO. On applying an electric field, the magnetoelastic effect of NiO is added to the total ME effect in this system via exchange coupling.

Expectedly, the vertical interfacial area between the matrix and column phases also appears to influence the ME effect. This is demonstrated by the following two points: (1) the ME coefficient in the NNN-32 sample is higher when grown on Nb:STO(111) ($1.5\times10^{-9}\,\mathrm{s\,m^{-1}}$) than on Nb:STO(001) ($1.11\times10^{-9}\,\mathrm{s\,m^{-1}}$), which is consistent with its larger vertical interfacial area (Supplementary Fig. 20); (2) the ME coefficient is higher for thicker samples (data for the 50 nm NNN-31 sample are shown in Supplementary Fig. 21).

Voltage-dependent in situ XRD measurements

To determine the strain coupling between the three phases in the nanocomposites, in situ XRD characterization was carried out in the NNN-31 film. Fig. 6a shows the XRD Omega-2Theta scan of the sample with different voltages applied (Supplementary Fig. 22 shows the full-range in situ XRD). Shifts of the NFO(004), NiO(002) and NBT(002) peaks are observed, verifying that the applied voltage in this sample has induced considerable strain in both NBT matrix phase and magnetic column phase. As shown in Fig. 6b, the peak position of the NiO–NFO phase changes from 43.358° to 43.299° when applying a voltage of −30 V ($1{,}500\,\mathrm{kV\,cm^{-1}}$). This peak shift corresponds to a vertical strain change of $\Delta\varepsilon_{100}=0.13\%$. Since no apparent peak broadening is observed from the Gaussian fit of the peak when applying the voltage, the strain change in both NFO and NiO is homogeneous. With the magnetoelastic coefficient for NFO, $\lambda_{100}=-50\times10^{-6}$ (ref. [30]), and the bulk Young's modulus, $Y=198\,\mathrm{GPa}$, for NFO (ref. [31]), the magnetoelastic energy associated with the strain can be obtained using $E=-3\lambda_{100}\Delta\sigma_{100}/2$, where the change in stress is given by $\Delta\sigma_{100}=Y\Delta\varepsilon_{100}$. This energy is calculated to be $E_{\mathrm{NFO}}=1.93\times10^5\,\mathrm{erg\,cm^{-3}}$. With a saturation magnetization value for bulk NFO of $M_{\mathrm{NFO}}=280\,\mathrm{emu\,cm^{-3}}$ (ref. [32]), we estimate $\Delta H_C=2E_{\mathrm{NFO}}/M_{\mathrm{NFO}}=1.38\,\mathrm{kOe}$. This roughly agrees with the change in H_C in our experiment, which was $\Delta H_C^{\mathrm{exp}}=0.81\,\mathrm{kOe}$.

The three-dimensional strain state in the NNN-31 sample was further studied using X-ray reciprocal space map (RSM) measurements around Nb:STO(113) and Nb:STO(103), as shown in Supplementary Fig. 23. While both NiO(113) and NFO(226) are present in the RSMs measured around Nb:STO(113), only the NFO(206) peak is present in the RSMs measured around Nb:STO(103), due to the systematic absence of the NiO(103) peak following the extinction rules[26]. Thus, the shift of the NFO(206) peak unambiguously shows the voltage-induced strain in the NFO phase. This strain can only be mediated by the NiO phase since the NFO phase is not directly attached to the NBT matrix. As shown in Supplementary Fig. 23b,d, when a voltage of −30 V is applied to the sample, the RSMs show a noticeable change in both NBT and NFO (+NiO) phases. A tail appears below the main peak of NBT(113) and NBT(103), in agreement with the peak broadening in the XRD Omega-2Theta scan shown in Fig. 6a. On application of a voltage, the position of NFO(206) and NFO(226) + NiO(113) peaks also shows a shift towards the negative Q_z direction. The lattice parameter of NiO was calculated from the RSM and listed in the table in Fig. 6c. It shows quite a large change in the OOP lattice parameter c and unnoticeable change in the IP lattice parameters a and b. The 'bulk' parameter is calculated by keeping the volume the same with the structure of 0 V. The c/a ratio of the NiO lattice is also listed in the table, which increases in the order of 0 V, −30 V and bulk.

DFT calculation of magnetic anisotropy energy

To get a deeper understanding of the strain-induced spin reorientation in the NiO, DFT calculations based on the experimental lattice parameters were carried out. We calculated the magnetic anisotropy energy (MAE) of the systems by rotating the magnetic moments in different magnetocrystalline planes. As shown in Fig. 6d–f, a weak MAE of about 55 μeV is obtained in NiO, where the (111) plane has the lowest energy compared with other planes, which agrees with the experimental results that NiO is an easy-plane AFM material. We also notice that both ours and other DFT calculations indicate the easy axes of NiO are along the $[\bar{1}10]$ directions lying in the (111) plane[33], which agrees with the experimental results of Roth[34,35], while most other experiments have suggested possible easy axes along the $[\bar{1}\bar{1}2]$ directions[36–38]. Thus, here we will only compare the strain-induced change in the MAE.

We can easily find two obvious changes in the MAE within the NiO with increasing c/a ratio. First, as the c/a ratio increases from 0.996 (0 V) to 1 (bulk), the easy-plane characteristic of the MAE is enhanced, with the energy of the OOP directions increasing steadily. More noticeably, there is a drastic increase in the energy along the [001] and $[00\bar{1}]$ directions. The uncompensated AFM spins tend to be aligned to the [001] directions by the exchange coupling to the FM NFO. An increase in energy in this direction will lower the probability of alignment in this direction and cause the AFM spins to rotate from higher to lower θ. This is one possible reason for the reduction in EB with applying an electric field in this system.

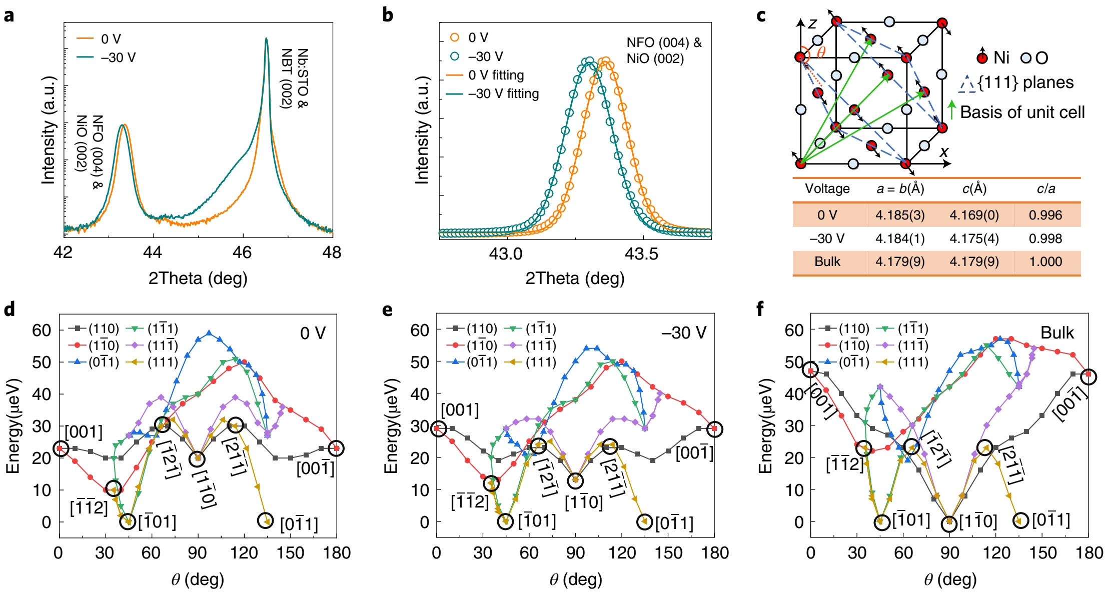

Voltage	$a = b$(Å)	c(Å)	c/a
0 V	4.185(3)	4.169(0)	0.996
–30 V	4.184(1)	4.175(4)	0.998
Bulk	4.179(9)	4.179(9)	1.000

Fig. 6 | Voltage-induced strain and its impact on magnetic anisotropy energy of NiO. a, XRD Omega-2Theta scan for the NNN-31 sample before and after the application of a voltage of –30 V between the Pt electrode and Nb:STO substrate. **b**, Shift of the overlapped NFO(004) and NiO(002) peaks under an applied voltage. The lines give the Gaussian fit of the data. **c**, Schematic of the magnetic structure of NiO and the lattice parameters obtained from X-ray RSMs. **d**–**f**, Magnetic anisotropy energy $E(\theta)$, calculated using the DFT method, for NiO of different lattice parameters given in **c**, calculated by rotating the Néel vector in different crystalline planes. The black circles indicate some of the high-symmetry directions.

Second, we also observe a remarkable change in the IP MAE with increasing c/a ratio. As compared in Supplementary Fig. 24, NiO (0 V) shows larger MAE, which tends to be biaxial in the (111) plane, with the energies in the $[\bar{1}01]$ and $[0\bar{1}1]$ directions much lower than that along the $[1\bar{1}0]$ direction due to symmetry breaking. As the c/a ratio increases (at –30 V), the energy of the $[1\bar{1}0]$ direction becomes smaller in NiO and finally equals to the energy of the $[\bar{1}01]$ and $[0\bar{1}1]$ directions in the NiO (bulk) with $c/a = 1$. The energy barrier between the $[\bar{1}01]$ ($[0\bar{1}1]$) direction and $[1\bar{1}0]$ direction is also reduced from 32 μeV in NiO (0 V) to 25 μeV in NiO (–30 V) and finally reaches 23 μeV in NiO (bulk). The decrease in the IP MAE and the emergence of triaxial anisotropy in NiO with high c/a ratio will also cause the IP spin reorientation from a higher to lower θ angle, which could be another reason for the reduced EB effect with applying an electric field. Moreover, with the MAE change between NiO (0 V) and NiO (–30 V), which is about 7 μeV, and the volume of the magnetic unit cell, that is, 36.5 Å^3, the change in MAE density in NiO is estimated to be $E_{\mathrm{NiO}} = 3.07 \times 10^5$ erg cm^{-3}. With a magnetoelastic coefficient of -140×10^{-6} (ref. [39]), and bulk Young's modulus $Y = 145$ GPa for NiO (ref. [40]), the anisotropy energy change can be calculated to be $E_{\mathrm{NiO}} = 3.96 \times 10^5$ erg cm^{-3}. These two values are in good agreement with each other.

The specific rotation angle of the AFM spins will depend on their initial alignment, and there are two possibilities. According to the DFT calculations, the uncompensated AFM spins are aligned to one of the $[\bar{1}01]$ directions in the (111) plane at 0 V. For this situation, the angle between these frozen spins and the cooling field will be $\theta_0 = 45°$. Assuming that the effective rotation of the Néel vector of NiO is $\delta\theta$, with applying a voltage of –30 V, we will have the following relation:

$$\frac{\delta H_{\mathrm{E}}}{H_{\mathrm{E0}}} = \frac{\cos\theta_0 - \cos(\theta_0 + \delta\theta)}{\cos\theta_0}$$

With the change in EB field, $\delta H_{\mathrm{E}} = 0.051$ kOe, and the initial EB field $H_{\mathrm{E0}} = -0.207$ kOe, we can roughly estimate that the uncompensated AFM spins are rotated by $\delta\theta \approx 12.8°$ at an applied voltage of –30 V. And if adopting $[\bar{1}\bar{1}2]$ as the initial direction of the frozen spins, the initial angle will be $\theta_0 = 35.3°$, and then a value of $\delta\theta \approx 16.7°$ will be obtained. It is noted that angle θ can only describe an average distribution of the AFM spins according to the Boltzmann distribution within the energy landscape. Thus, $\delta\theta$ describes the average change in the distribution.

Conclusions

We have reported room-temperature self-biased ME switching in a three-phase FE–AFM–FM vertically aligned nanocomposite thin-film system of NBT–NiO–NFO. NBT forms the film matrix with vertical NiO-coated NFO nanocolumns embedded in it. The system is grown in a one-step growth process, without complex multilayer fabrication. The switching process involves changing the magnetic anisotropy from perpendicular to IP direction, and this produces a self-biased ME coefficient of up to 1.38×10^{-9} s m^{-1} at room temperature. By applying –30 V, the anisotropy energy K_{eff} of this system changes from 0.91×10^4 J m^{-3} (easy axis) to -1.65×10^4 J m^{-3} (easy plane).

The large self-biased ME effect is due to three key factors. First, the presence of the NiO phase leads to a reduction in the leakage compared with a typical two-phase system comprising NBT and NFO. This is because when NiO is present, it coats the NFO, ensuring an NBT interlayer forming between the NiO and Nb:STO substrate, leading to a current-blocking p–n junction at the NBT–Nb:STO interface. In the absence of NiO, NFO contacts the Nb:STO, which does not form a current-blocking junction. Second, the soft-magnetic characteristics of NFO lead to a self-biased ME effect, which is further enhanced by the room-temperature EB effect in the NiO–NFO AFM–FM columns. Finally, the intermediate AFM NiO shell has a higher magnetoelastic coefficient and adds to the magnetic anisotropy change in the NFO through its coupling to the FE NBT, which is strained by the electric field and hence further enhances the converse ME effect. DFT calculations confirm our findings of the magnetoelastic effect of the NiO induced by strain change, which agrees with the voltage evolution of the EB effect. Our three-phase composite film system could be of use in the development of room-temperature ME memory and microsensor devices.

Methods

Sample preparation. Self-assembled NBT–NFO, NBT–NiO–NFO nanocomposite thin films and NBT films were grown from a single ceramic target, on 0.5 wt.% Nb-doped $SrTiO_3$ (Nb:STO) (001) and (111) substrates, by pulsed laser deposition. A KrF laser ($\lambda = 248$ nm) was used with a fluence of 1.3 J cm^{-2} and a repetition rate of 5 Hz. The growth rate was about 2 nm min^{-1}. During the deposition, the substrate temperature was 680 °C. To ensure oxygen stoichiometric NBT in the nanocomposites, a relatively high O_2 atmosphere of 0.3 mbar was adopted during the deposition. Polycrystalline NBT–NFO and NBT–NiO–NFO composite targets were synthesized using solid-state sintering from high-purity sodium carbonate (Na_2CO_3), bismuth oxide (Bi_2O_3), titanium dioxide (TiO_2), iron III oxide (Fe_2O_3) and nickel oxide (NiO) powders from Sigma Aldrich (99.99% purity). An excess of 10% for both Bi and Na elements was adopted to avoid chemical deficiencies at the A site, ensuring a stoichiometric NBT phase. The final sintering of the target was performed at 1,100 °C for 2 h.

Structural characterization. The stoichiometry of a pure NBT and an NBT–NiO–NFO (4:3:1) film was checked with RBS using a 4 MeV $^4He^+$ ion beam from a 3 MV pelletron tandem ion accelerator. The stoichiometry was determined by fitting the measured RBS spectrum with a well-known SIMNRA simulation code. XRD experiments were carried out with a Panalytical Empyrean high-resolution X-ray diffractometer with a hybrid primary monochromator ($\lambda = 1.5405$ Å). RSMs with in situ electric field were measured with a pixel detector, which enables both high speed and high resolution. A Pt layer covering around 80% of the surface of the sample (that is, 4.5 × 4.5 mm^2 for Pt electrode versus 5 × 5 mm^2 for the sample surface) was deposited using sputtering and served as the top electrode, and the Nb:STO substrate served as the bottom electrode. During the in situ XRD and RSM measurements, an electric field was applied between the Pt electrode and Nb:STO substrate with a Keithley 2400 sourcemeter. The surface morphology was characterized using an atomic force microscope (Multimode 8 SPM with NanoScope V controller). PFM was performed with an Agilent 5500 scanning probe microscope using different tips, a diamond-coated silicon tip and a Pt-coated silicon tip. Further, c-AFM was performed with the same setup with a Pt-Ir tip. Cross-sectional scanning transmission electron microscopy (STEM) and energy-dispersive X-ray spectroscopy (EDX) were used to characterize the microscopic structure and elemental distributions of the film.

Measurements. The magnetic properties and converse ME effect was measured with an MPMS3 (Quantum Design). During the ME measurements, an electric field was applied between the Pt electrode and Nb:STO substrate with a Keithley 2400 sourcemeter. The current density (J) versus electric field (E) curves were measured with a Keithley 2400 sourcemeter controlled by the LabVIEW program. Hall measurements of the NBT film were carried out using a PPMS (Quantum Design) interfaced to a Keithley 2182 nanovoltmeter and 2425 sourcemeter.

DFT calculations. The DFT calculations were carried out using the Vienna ab initio simulation package (VASP). In the calculation of the MAE of NiO, we used projector-augmented plane-wave pseudopotentials with valence configuration [Ar]$3d^84s^2$ for Ni and [Ar]$2s^22p^4$ for O, and a plane-wave energy cutoff of 450 eV. In the calculations, the magnetic unit cell of rocksalt NiO (space group $Fm\bar{3}m$) with basis vectors shown in Fig. 6c was adopted. The corresponding Brillouin zones are sampled by a Gamma-centred mesh of $4 \times 4 \times 4\, k$ points. The total free energy $E(\theta, \varphi)$ was calculated with θ and φ being the angle between of the Néel vector and $+z$ direction and the angle between the projection of the Néel vector in the x–y plane and $+x$ direction, respectively. The trajectory of rotation of the Néel vector was restricted in the high-symmetry planes, such as (111) and (110) planes. In the calculations, an on-site Coulomb repulsion term $U = 5$ eV was used to give proper magnetic properties of NiO (ref. [41]); this is demonstrated using a calculation with $U = 8$ eV (Supplementary Fig. 25). Considering that NiO can perform a slight rhombohedral deformation, the results are also checked by a calculation based on rhombohedral NiO (space group $R\bar{3}m$; $\alpha = 90.09°$). Although the (111) and ($11\bar{1}$) planes become non-degenerate due to symmetry breaking in rhombohedral NiO, the calculated MAE shows a similar trend as that of the cubic phase, as shown in Supplementary Fig. 24b. In the calculation of the binding energy of NiO–STO, NBT–STO, NiO–NBT and NFO–NBT interfaces, we have only considered the (001)-oriented layers for the sake of simplicity, and these are indeed the orientations that we observed at the film–substrate interfaces. In the calculation, two steps were followed. First, we optimize the lattice structure of NiO, NFO, STO and NBT individual layers. Then, we combine any two of them to form the stacks, that is, NiO–STO, NBT–STO, NiO–NBT and NFO–NBT. The stacks have different lattice planes meeting at the interface, for example, as stack 1 and stack 1' for the NiO–STO stacks, as shown in Supplementary Fig. 7, and then optimize the lattice structures of the stacks. Although NBT shows some lattice distortion after lattice optimization (due to the ordered Na/Bi occupation, which is random in real materials), no apparent geometry distortion was observed in the second optimization, which enables us to subtract the interface binding energies E_b. E_b is defined as $E_b = E_1 + E_2 - E_{stack}$, where E_1 and E_2 represent the energies of two individual layers and E_{stack} is the stack's energy.

Data availability

The data that support the plots within this paper and other findings of this study are available from the corresponding authors upon reasonable request.

Received: 30 April 2020; Accepted: 20 April 2021;
Published online: 25 May 2021

References

1. Ramesh, R. & Spaldin, N. A. Multiferroics: progress and prospects in thin films. *Nat. Mater.* **6**, 21–29 (2007).
2. Spaldin, N. A. & Ramesh, R. Advances in magnetoelectric multiferroics. *Nat. Mater.* **18**, 203–212 (2019).
3. Wang, K. L., Lee, H. & Amiri, P. K. Magnetoelectric random access memory-based circuit design by using voltage-controlled magnetic anisotropy in magnetic tunnel junctions. *IEEE Trans. Nanotechnol.* **14**, 992–997 (2015).
4. Hill, N. A. Why are there so few magnetic ferroelectrics? *J. Phys. Chem. B* **104**, 6694–6709 (2000).
5. Vaz, C. A. F., Hoffman, J., Ahn, C. H. & Ramesh, R. Magnetoelectric coupling effects in multiferroic complex oxide composite structures. *Adv. Mater.* **22**, 2900–2918 (2010).
6. Chen, A., Su, Q., Han, H., Enriquez, E. & Jia, Q. Metal oxide nanocomposites: a perspective from strain, defect, and interface. *Adv. Mater.* **31**, 1803241 (2019).
7. Zheng, H. et al. Multiferroic $BaTiO_3$-$CoFe_2O_4$ nanostructures. *Science* **303**, 661–663 (2004).
8. Nan, C.-W., Liu, G., Lin, Y. & Chen, H. Magnetic-field-induced electric polarization in multiferroic nanostructures. *Phys. Rev. Lett.* **94**, 197203 (2005).
9. Liu, G., Nan, C.-W. & Sun, J. Coupling interaction in nanostructured piezoelectric/magnetostrictive multiferroic complex films. *Acta Mater.* **54**, 917–925 (2006).
10. Zavaliche, F. et al. Electric field-induced magnetization switching in epitaxial columnar nanostructures. *Nano Lett.* **5**, 1793–1796 (2005).
11. Nogue, J. & Schuller, I. K. Exch'ange bias. *J. Magn. Magn. Mater.* **192**, 203–232 (2002).
12. Jungwirth, T. et al. The multiple directions of antiferromagnetic spintronics. *Nat. Phys.* **14**, 200–203 (2018).
13. Dix, N. et al. On the strain coupling across vertical interfaces of switchable $BiFeO_3$–$CoFe_2O_4$ multiferroic nanostructures. *Appl. Phys. Lett.* **95**, 062907 (2009).
14. Wu, R. et al. Design of a vertical composite thin film system with ultralow leakage to yield large converse magnetoelectric effect. *ACS Appl. Mater. Interfaces* **10**, 18237–18245 (2018).
15. Zhang, J. X. et al. A novel nanostructure and multiferroic properties in $Pb(Zr_{0.52}Ti_{0.48})O_3/CoFe_2O_4$ nanocomposite films grown by pulsed-laser deposition. *J. Phys. D.* **41**, 235405 (2008).
16. Kim, D. H., Ning, S. & Ross, C. A. Self-assembled multiferroic perovskite–spinel nanocomposite thin films: epitaxial growth, templating and integration on silicon. *J. Mater. Chem. C* **7**, 9128–9148 (2019).
17. Zheng, H. et al. Self-assembled growth of $BiFeO_3$–$CoFe_2O_4$ nanostructures. *Adv. Mater.* **18**, 2747–2752 (2006).
18. Eshghinejad, A. et al. Piezoelectric and piezomagnetic force microscopies of multiferroic $BiFeO_3$-$LiMn_2O_4$ heterostructures. *J. Appl. Phys.* **116**, 066805 (2014).
19. Wang, L. et al. Interfacial strain driven magnetoelectric coupling in (111)-oriented self-assembled $BiFeO_3$–$CoFe_2O_4$ thin films. *J. Mater. Chem. C* **8**, 3527–3535 (2020).
20. Zhang, K. H. L. et al. Electronic structure and band alignment at the NiO and $SrTiO_3$ p–n heterojunctions. *ACS Appl. Mater. Interfaces* **9**, 26549–26555 (2017).
21. Yi, D. et al. Tuning perpendicular magnetic anisotropy by oxygen octahedral rotations in $(La_{1-x}Sr_xMnO_3)/(SrIrO_3)$ superlattices. *Phys. Rev. Lett.* **119**, 077201 (2017).
22. Johnson, M. T., Bloemen, P. J. H., Broeder, F. J. A. D. & Vries, J. J. D. Magnetic anisotropy in metallic multilayers. *Rep. Prog. Phys.* **59**, 1409–1458 (1996).
23. Zhang, J. et al. The magnetization reversal mechanism in electrospun tubular nickel ferrite: a chain-of-rings model for symmetric fanning. *Nanoscale* **11**, 13824–13831 (2019).
24. Shirahata, Y. et al. Electric-field switching of perpendicularly magnetized multilayers. *NPG Asia Mater.* **7**, e198 (2015).
25. Hu, J.-M. et al. Purely electric-field-driven perpendicular magnetization reversal. *Nano Lett.* **15**, 616–622 (2015).
26. Wu, R. et al. All-oxide nanocomposites to yield large, tunable perpendicular exchange bias above room temperature. *ACS Appl. Mater. Interfaces* **10**, 42593–42602 (2018).
27. Lage, E. et al. Exchange biasing of magnetoelectric composites. *Nat. Mater.* **11**, 523–529 (2012).

28. Ahlawat, A. et al. Electric field poling induced self-biased converse magnetoelectric response in PMN-PT/$NiFe_2O_4$ nanocomposites. *Appl. Phys. Lett.* **111**, 262902 (2017).
29. Meiklejohn, W. H. & Bean, C. P. New magnetic anisotropy. *Phys. Rev.* **105**, 904–913 (1957).
30. Fritsch, D. & Ederer, C. First-principles calculation of magnetoelastic coefficients and magnetostriction in the spinel ferrites $CoFe_2O_4$ and $NiFe_2O_4$. *Phys. Rev. B* **86**, 014406 (2012).
31. Fritsch, D. & Ederer, C. Epitaxial strain effects in the spinel ferrites $CoFe_2O_4$ and $NiFe_2O_4$ from first principles. *Phys. Rev. B* **82**, 104117 (2010).
32. Chong, Y. T., Yau, E. M. Y., Nielsch, K. & Bachmann, J. Direct atomic layer deposition of ternary ferrites with various magnetic properties. *Chem. Mater.* **22**, 6506–6508 (2010).
33. Schrön, A., Rödl, C. & Bechstedt, F. Crystalline and magnetic anisotropy of the 3*d*-transition metal monoxides MnO, FeO, CoO, and NiO. *Phys. Rev. B* **86**, 115134 (2012).
34. Roth, W. L. Neutron and optical studies of domains in NiO. *J. Appl. Phys.* **31**, 2000–2011 (1960).
35. Roth, W. L. Multispin axis structures for antiferromagnets. *Phys. Rev.* **111**, 772–781 (1958).
36. Uchida, E. et al. Magnetic anisotropy of single crystals of NiO and MnO. *J. Phys. Soc. Jpn* **23**, 1197–1203 (1967).
37. Kondoh, H. & Takeda, T. Observation of antiferromagnetic domains in nickel oxide. *J. Phys. Soc. Jpn* **19**, 2041–2051 (1964).
38. Machado, F. L. A. et al. Spin-flop transition in the easy-plane antiferromagnet nickel oxide. *Phys. Rev. B* **95**, 104418 (2017).
39. Phillips, T. G. & White, R. L. Single-ion magnetostriction in the iron group monoxides from the strain dependence of electron-paramagnetic-resonance spectra. *Phys. Rev.* **153**, 616–620 (1967).
40. Fasaki, I., Koutoulaki, A., Kompitsas, M. & Charitidis, C. Structural, electrical and mechanical properties of NiO thin films grown by pulsed laser deposition. *Appl. Surf. Sci.* **257**, 429–433 (2010).
41. Bengone, O., Alouani, M., Blöchl, P. & Hugel, J. Implementation of the projector augmented-wave LDA+U method: application to the electronic structure of NiO. *Phys. Rev. B* **62**, 16392–16401 (2000).

Acknowledgements

We acknowledge funding from the Leverhulme Trust grant no. RPG-2015-017, EPSRC grant nos. EP/N004272/1 and EP/M000524/1, the Royal Academy of Engineering Chair in Emerging Technologies grant no. CiET1819\24, EU grant no. H2020-MSCA-IF-2016 (745886)-MuStMAM and the Isaac Newton Trust (grant no. RG96474). This work was supported by the National Key R&D Program of China (grant no. 2017YFA0206303) and the National Natural Science Foundation of China (grant nos. 11975035 and 51731001). The US–UK collaborative effort was funded by the U.S. National Science Foundation grant nos. ECCS-1902644 (Purdue University) and ECCS-1902623 (University at Buffalo, SUNY), U.S. Office of Naval Research grant no. N00014-20-1-2043 (Purdue University) and the EPRSC grant no. EP/T012218/1 (University of Cambridge).

Author contributions

R.W. and J.L.M.-D. conceived the experiments and supervised the research. R.W. made the samples and carried out the XRD and AFM characterizations and magnetic properties measurement. D.Z., P.L., X.G. and H.W. performed STEM imaging and EDX mapping. Jie Yang, R.W., G.T., Z.R. and Jinbo Yang contributed to the DFT calculation. S.Z., Z.Z. and M.L. contributed to the FMR measurement. X.W., H.Z. and Q.J. contributed to the Hall effect measurement. A.K. contributed to the PFM and c-AFM measurements. Y.W. and W.L. contributed to the RBS characterization. R.W., C.Y. and K.H.L.Z. contributed to the electric measurement and analysis. R.W., T.M. and J.L.M.-D. contributed to the data analysis and wrote the manuscript. All the authors contributed to reviewing and revising the manuscript.

Competing interests

The authors declare no competing interests.

Additional information

Supplementary information The online version contains supplementary material available at https://doi.org/10.1038/s41928-021-00584-y.

Correspondence and requests for materials should be addressed to R.W., T.M. or J.L.M.-D.

Peer review information *Nature Electronics* thanks Morgan Trassin and the other, anonymous, reviewer(s) for their contribution to the peer review of this work.

Reprints and permissions information is available at www.nature.com/reprints.

Publisher's note Springer Nature remains neutral with regard to jurisdictional claims in published maps and institutional affiliations.